ADVANCED FUNCTIONAL MATERIALS
www.afm-journal.de

Near-Field Optical Detection of Defect-Stabilized Metallic Islands at the Verwey Transition in Fe_3O_4

*Kajal Tiwari, Mostafa Ibrahim Shehata Marzouk, Ke Xiao, Malleswararao Tangi, and Stuart Stephen Papworth Parkin**

Magnetite (Fe_3O_4) undergoes a metal-to-insulator transition (MIT) at the Verwey transition that is accompanied by significant structural distortions. This archetypical transition is extensively studied due to its highly correlated nature. Here, the formation of defect-stabilized metallic islands is shown at the MIT that we directly image using high-resolution scattering-type scanning near-field optical microscopy in the mid-infrared (MIR) to terahertz (THz) spectral range. The transition to the insulating state on cooling is accompanied by the formation of remnant metallic islands just a few hundred nm in extent within less than 1 K of the MIT. Notably, these islands occur at similar places on repeated cooling cycles, suggesting the presence of pinning centers. Temperature-dependent low-frequency MIR and THz optical responses show a similarly sharp MIT, indicating a clear first-order transition. On the other hand, as compared to the MIR signal, a reduction in the THz signal at temperatures above the MIT is indicative of short-range ordering consistent with the formation of polarons. The findings highlight the importance of nanoscale optical imaging in understanding the electronic properties of strongly correlated materials.

1. Introduction

Magnetite, a strongly correlated ferrimagnet with a cubic inverse spinel structure,[1] undergoes a first-order Verwey transition upon cooling below the Verwey temperature (T_V) characterized by an abrupt decrease of the DC conductivity by two orders of magnitude.[2,3] The origin of the metal-to-insulator transition (MIT) in Fe_3O_4 has been attributed to an intricate interplay between electronic charge, phonons and orbital interactions encompassing charge ordering of the Fe^{2+} and Fe^{3+} ions,[3] a trimeron lattice formation due to complex charge orbital ordering in the low-temperature phase,[4,5] and a recently proposed electron-phonon coupling of the high-temperature phase electron nematicity and the low-temperature trimeron ordering.[6]

Local defects and lattice strain play pivotal roles in crafting the physical properties of magnetite due to strong interactions between phonons and electronic charge fluctuations.[7] Moreover, first-principle calculations have demonstrated that the electronic structure of Fe_3O_4 is tunable by strain which directly affects the trimeron formation, consequently altering the transition temperature.[8] Hence, investigating the dynamics of the transition spatially would be very helpful in uncovering the underlying regulating mechanisms behind the MIT. Existing work has suggested a phase-separated state but lacks a direct visualization of the spatial intricacies expected for the predicted percolative nature[5] of the first-order transition in magnetite.

Scattering-type scanning near-field optical microscopy (s-SNOM)[9,10] is a unique capability for non-contact, non-destructive optical imaging to provide direct spatial visualization, beyond the diffraction limit. A sharp metallic tip under illumination by a focused laser beam acts as a plasmonic nanoprobe for electric fields polarized along the tip axis (see **Figure 1a**).[11] The light scattered by the tip working in the tapping mode in close proximity to the sample is detected. The tip scattered near-field signal is a result of a high-order nonlinear tip-sample interaction that arises from the sample dielectric response from the volume directly beneath the tip, offering a spatial resolution both in area and volume down to nanometer length scales, constrained only by the curvature of the tip. s-SNOM has been successfully employed to explore phase change materials such as VO_2,[12] TaS_2,[13] polaritonic configurable nano-optics,[14] metasurfaces,[15] ferroelectricity,[16] as well as to carry out magnetic domain imaging,[17] and charge carrier density mapping.[18]

In this paper, we utilize cryogenic s-SNOM to investigate the nanoscale mid-infrared (MIR) and terahertz (THz)[19,20] reflectivity of a Fe_3O_4 film as the film undergoes the first-order Verwey transition on cooling down below 114 K. Notably, in the MIR excitation wavelengths, a non-uniform structure where the high-temperature phase becomes an array of disconnected metallic islands within an insulating matrix, is identified. The islands exhibit diffuse boundaries with an

K. Tiwari, M. I. S. Marzouk, K. Xiao, M. Tangi, S. S. P. Parkin
Max Planck Institute for Microstructure Physics
Weinberg 2, 06120 Halle (Saale), Germany
E-mail: stuart.parkin@mpi-halle.mpg.de

The ORCID identification number(s) for the author(s) of this article can be found under https://doi.org/10.1002/adfm.202507075

© 2025 The Author(s). Advanced Functional Materials published by Wiley-VCH GmbH. This is an open access article under the terms of the Creative Commons Attribution License, which permits use, distribution and reproduction in any medium, provided the original work is properly cited.

DOI: 10.1002/adfm.202507075

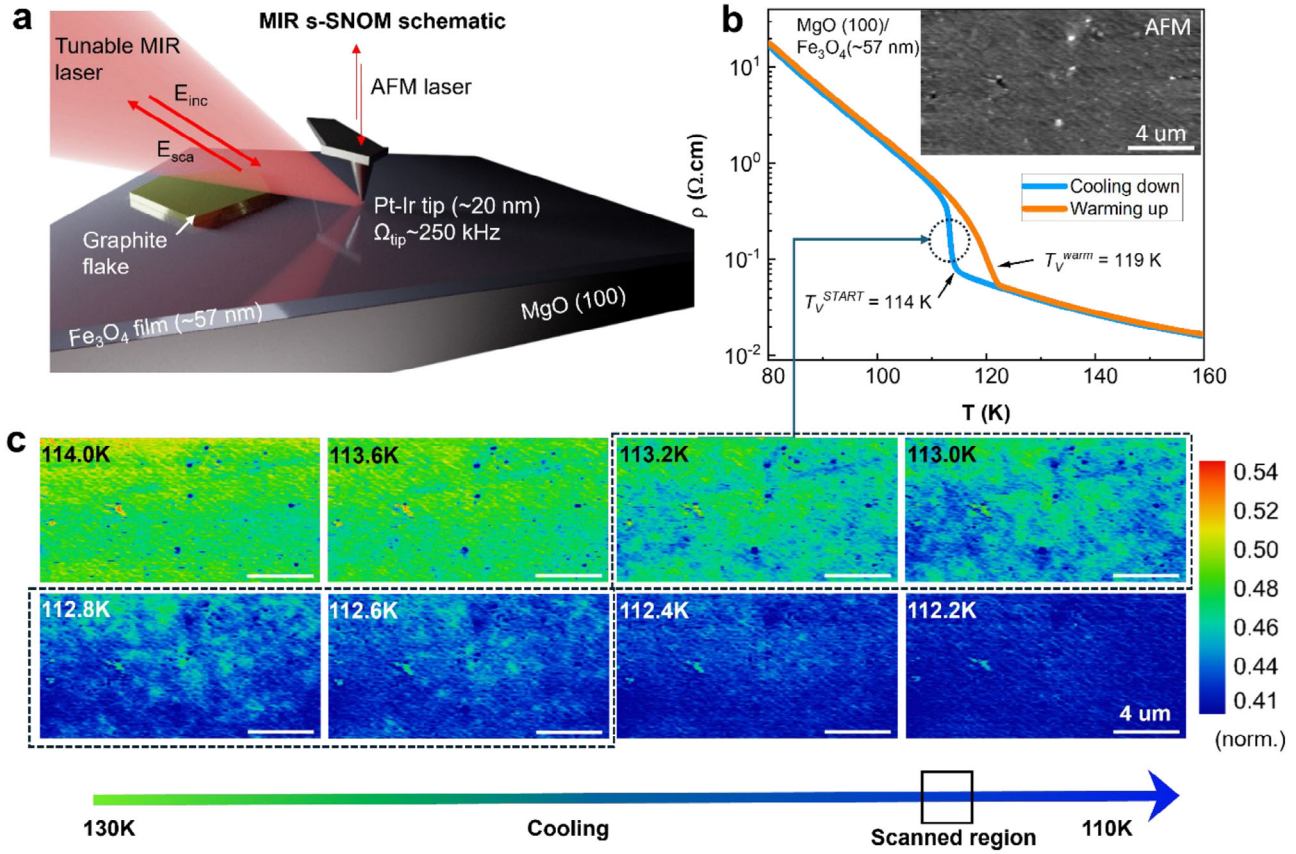

Figure 1. Near-field imaging of the MIT in magnetite. a) Experimental schematic of the MIR s-SNOM setup. b) Resistance versus temperature curve for Fe_3O_4 showing a hysteretic behavior typical of a first-order transition. The inset shows an AFM image of the film, revealing a high-quality surface with well-defined terraces. c) s-SNOM scattered electric field (amplitude) images at an excitation wavenumber of 900 cm^{-1}. The signal is demodulated at the 3rd harmonic (S_{3A}) of the tip oscillation frequency. The MIT in Fe_3O_4 probed during the cooling cycle; at the onset of the transition below 114.0 K, inhomogeneity starts to appear around 113.2 K forming remnant metallic islands (green, higher signal) within an insulating matrix (blue, lower signal) most prominent at 113.0 K. As the sample temperature goes below 113.0 K, the number of islands decreases. At 112.2 K, an insulating phase prevails, resulting in a uniform signal throughout. All the images are normalized with a graphite flake that is scanned simultaneously. Scale bar: 4 μm.

approximate radius below 500 nm, and intriguingly, their consistent emergence across repeated cooling cycles suggests the role of local pinning centers which delay the freezing-in to the insulating state. s-SNOM nano-imaging with different MIR illumination frequencies reveals a distinct contrast between the insulating and metallic phases that are particularly pronounced at lower frequencies. Low wavenumber MIR (900 cm^{-1}, equivalent to ≈112 meV) and THz (2–8 meV) reflectivity uncovers a sharp transition, indicative of an optical gap associated with the formation of an insulating trimeron network.[21] A fast decrease in the THz signal as the film approaches the MIT from the high-temperature state indicates the presence of low-energy charge carriers with a diminishing mobility as the transition nears. This supports the previously reported polaron-hopping type conductivity where the polarons (or trimerons), which form an ordered insulating lattice below the transition, exist as dissociated domains above the transition and cause hopping-type charge transport at picosecond timescales.[5,21,22]

2. Results and Discussion

s-SNOM imaging was performed on a 57 nm thick magnetite thin film grown on a MgO (100) substrate using state-of-the-art molecular beam epitaxy (MBE) (see Figure 1a for the experimental setup). X- ray diffraction (XRD) characterization shows the epitaxial growth of the Fe_3O_4 film (see SI Note 1, Supporting Information) and X-ray reflectivity (XRR) measurements indicate a good homogeneity and a high crystalline quality of the film. Figure 1b illustrates the resistivity of the film as it undergoes a metal-to-insulator transition starting at $T_v^{START} \approx 114$ K and ending near 112 K during the cooling cycle while the change in resistivity while warming up is over a slightly broader temperature interval. This hysteretic behavior is typical of a first-order Verwey transition.[23] The inset of Figure 1b shows an atomic force microscopy (AFM) image of the film, revealing a high-quality surface with well-defined terraces.

Temperature-dependent spatial maps of the 3rd order tip-demodulated s-SNOM amplitude from the Fe_3O_4 film

© 2025 The Author(s). Advanced Functional Materials published by Wiley-VCH GmbH

measured at a MIR excitation wavenumber 900 cm^{-1} are summarized in Figure 1c (see Methods for experimental details). In s-SNOM, the detected signal contains several harmonics of the tip-scattered field (S_n); higher harmonics (n = 2 and above) provide a background-free response, and thus the 3rd harmonic was used for our analysis. A pseudo-heterodyne interferometric detection scheme was employed to separate the amplitude (S_{3A}) and phase (S_{3P}) components of the scattered signal.[24] For the measurements, the film was cooled down from 130 K which is a few K above the warming-up transition temperature. As shown in the figure, the s-SNOM signal is homogenous over the scanned region (≈25 × 10 μm^2) at T_v^{START}. As the transition reaches the midway point, a distinct intermediate state emerges, characterized by metallic islands (green/higher signal) anchored within an insulating (blue/lower signal) matrix. The islands continue to shrink and decrease in number at later stages of the transition. At 112.2 K, which marks the end of the transition, a uniform low contrast of the signal is observed all over the scanned region confirming the complete transition of the film to an insulating phase. Here, the high-temperature state which exhibits a semi-metallic behavior[25,26] is referred to as the metallic state throughout the paper in the context of the MIT.

To understand the driving mechanism(s) behind the anchoring of islands during the transition, we perform s-SNOM imaging of the intermediate state during two different cooling cycles, as shown in **Figure** 2a,b. Interestingly, the areas where the islands are anchored remain nearly the same. To quantitatively confirm this visual similarity, we compared the two images using the Structural Similarity Index (SSIM) analysis,[27] as illustrated in Figure 2c. SSIM evaluates local luminance, contrast, and structural correlations between images, providing a similarity index typically ranging from 0 (low similarity) to 1 (exact match). The overall SSIM score obtained was 0.97, indicating excellent structural similarity between the images. This observation emphasizes the role of local pinning defects that give rise to a phase-separated state. In Figure 2d, a single isolated island with a radius of ≈500 nm in the insulating matrix is marked with a white dashed circle. The corresponding AFM (grayscale) shows no significant topography at the island location, affirming that the island is solely a result of the anchored residual metallic phase. We find that the edges of the terraces of the epitaxial Fe_3O_4 film (ranging from ≈200 to ≈500 nm) (refer to SI Note 1, Supporting Information for an AFM image) appear bright in the s-SNOM images, but do not appear to have any correlation with the island locations.

In some materials, the complex s-SNOM signal dependence on the excitation frequency may not be straightforward, potentially resulting in a reversal of contrast of the metallic and insulating states for specific frequencies either in amplitude or phase or both.[28] Hence, it is important to look at both the amplitude and phase of the scattered signal to correctly determine the behavior of the real and imaginary parts of the dielectric response of a material. In the s-SNOM phase image shown in Figure 2e, the presence of islands is evident in phase and matches the amplitude images of Figure 2a,b. To elucidate the aforementioned observations and to gain a broader understanding of the complex s-SNOM signal across a wider spectrum of MIR frequencies beyond those examined in our experiment, we conducted analytical calculations based on the far-field optical parameters, employing a finite dipole model.[9,29] This model assumes the tip to be a metallic dipole sphere with a radius defined by the tip radius of curvature. The differences between the high-temperature ($T > T_V$) and low-temperature phases ($T < T_V$) in the amplitude and phase of the scattered signal are summarized in SI Note 5, Supporting Information. Our calculations indicate that the complex s-SNOM signal of Fe_3O_4 exhibits a straightforward frequency dependency within a narrow window of distinct contrast between the two states. Consequently, one could anticipate a stronger signal in amplitude and higher phase for the metallic state and a diminishing contrast between the metallic and insulating states at higher frequencies. Furthermore, the calculated amplitudes have enhanced contrast between the two states at higher harmonics. These calculations are consistent with our experimental observations, as discussed later.

We performed an estimation of the island sizes in the intermediary state, as shown in Figure 2f. We found that the islands of radii less than 500 nm are dominant in this state. At lower temperatures, islands shrink in size and decrease in number resulting in a noticeable shift in the size distribution. This shift is evident from the derived parameters of the Gaussian fitting applied to the island size distribution. The estimation of island sizes across repeated cooling cycles reveals a consistent similarity in both size and count (see SI Note 2, Supporting Information). In addition, the islands generally exhibit diffuse boundaries. It is likely that a gradual stepwise cool-down procedure (see SI Note 6, Supporting Information) in this metastable transformational temperature regime allows for an organization of islands into the lowest-energy configuration. This could be understood, based on studies of MITs in other materials,[30] as a competition between a long-range ordered trimeron lattice in the insulating phase and a charge fluctuating metallic state in Fe_3O_4.[5,22] The islands demonstrate some degree of isotropy in the shape unlike directional percolative structures observed in strained manganites.[31]

To obtain a comprehensive understanding of the MIT when investigated at various energy regimes below the Fermi level, we compare the s-SNOM reflectivity at MIR and THz frequency ranges. Quasiparticles, such as trimerons, represent low-energy phenomena, especially noticeable in the THz frequency range, particularly when studying metal-insulator transitions.[32–35] THz s-SNOM stands out as particularly useful in this regard, providing excellent sensitivity to subtle charge carrier dynamics and the ability to distinguish between different quasiparticles with unique mobilities. Consequently, it offers a valuable approach to understanding the details of DC transport characteristics linked to metal-insulator transitions.[36] We employ a broadband THz source spanning from 0.1 to 2 THz which excites the sample in the form of picosecond long pulses. The collected THz s-SNOM signal corresponds to the amplitude of the peak of the scattered THz broadband pulse to give a dielectric response of the sample.[19] The signal is obtained at the 2nd order of the tip dither frequency to eliminate background scattering.

THz s-SNOM imaging conducted within the same region of interest as for the MIR image shown in Figure 2a,b, shows no evident island formation (see **Figure** 3a). There are tiny speckles visible at temperatures in the vicinity of the transition (114.2 to 112.8 K). However, it is challenging to determine whether they are a result of a short-range phase segregation or a noisy

© 2025 The Author(s). Advanced Functional Materials published by Wiley-VCH GmbH

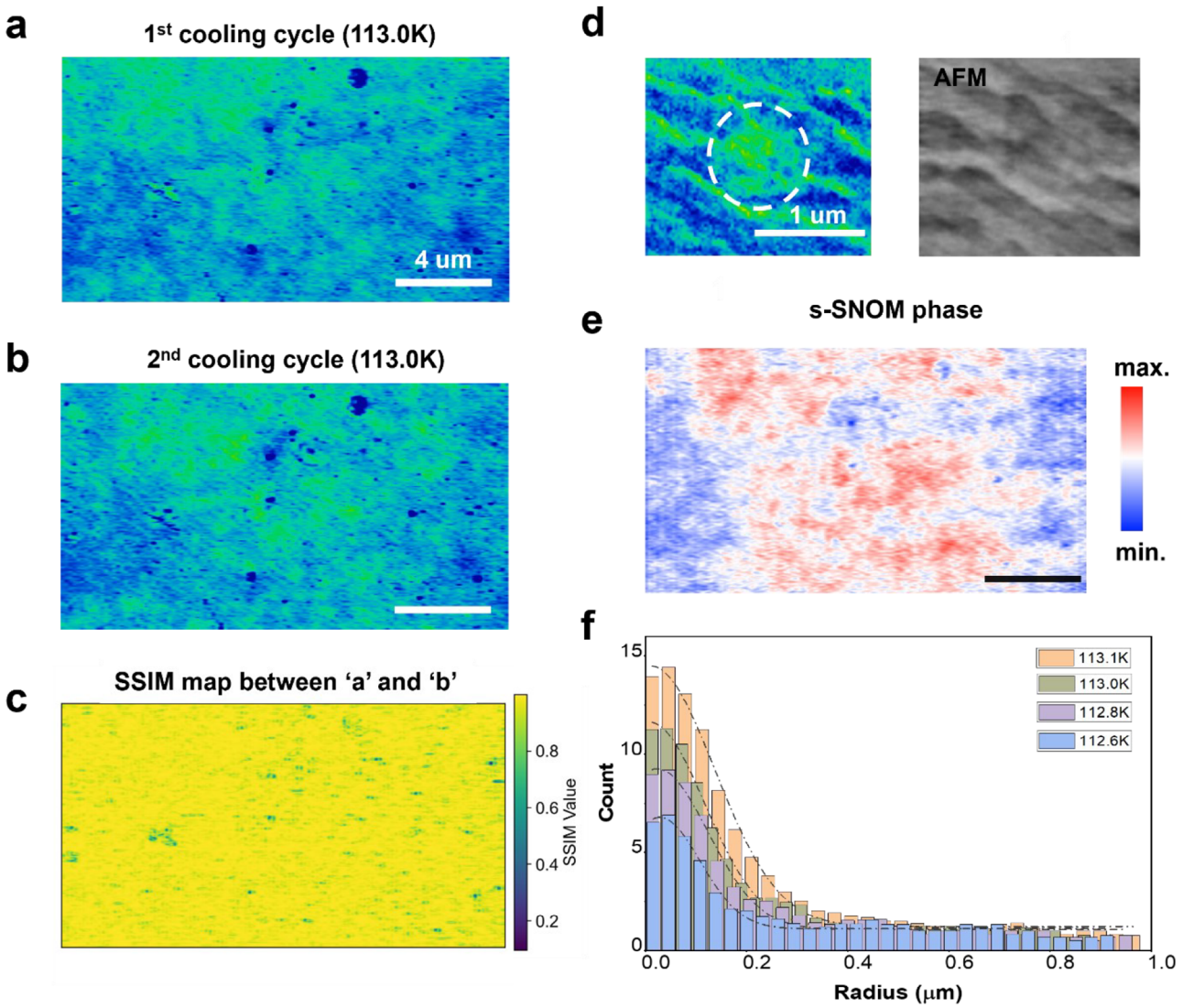

Figure 2. Origin of island formation, phase information, and estimation of island size in the transition state. a,b) Metallic islands in the same scanned area of the film for two different cooling cycles. c) The Structural Similarity Index (SSIM) analysis between the images presented in a) and b) shows a high similarity score, confirming a strong structural resemblance. Similar locations of islands suggest local defects or inhomogeneities aiding the forming of the islands in the transition state. d) s-SNOM image of single island and corresponding AFM (grayscale). AFM image shows no topography change at the island location. Images are taken at an excitation wavenumber of 900 cm^{-1}. e) The s-SNOM phase image (S_{3P}) correlates with the amplitude images as predicted from analytical calculations using a finite dipole model (see SI Note 5, Supporting Information). f) Island size estimation using best-fit circles via signal threshold detection (see SI Note 2, Supporting Information for further details). The number of islands (count) versus their radius (μm) is shown for four different temperatures during a cooling cycle.

signal. Furthermore, we see a strong signal in the film closer to an exfoliated graphite flake that was placed on the Fe_3O_4 film as a reference. This signal diminishes over the course of the transition. We believe this observation cannot be considered as a signal change from the transition itself since the strong signal exists over a wide range of temperature. The spectral characteristics of the scattered THz signal are provided in SI Note 9, Supporting Information. The overall signal-to-noise ratio of the collected THz reflectivity is compromised by factors such as power loss in optical windows and the attenuation of the THz waves in air. To address the low signal-to-noise ratio (SNR) in the THz signal and extract meaningful data, we perform wide-area averaging of the same area on the film (see SI Note 8, Supporting Information) distant from the graphite for both MIR and THz reflectivity and then compare the results. In Figure 3b, a comparison of the average MIR and THz s-SNOM reflectivity versus temperature is performed. The shaded area indicates the standard deviation (SD) of the average signal (see Methods). The signal is normalized [from 0 to 1] for comparison. The MIR s-SNOM signal shows a subtle decrease from 130 K to T_V followed by a sharp drop to a lower value during the transition, and subsequently, a gradually decreasing signal after the transition as the temperature is further lowered. A sharp drop in the signal during the transition is expected since the sample's resistivity increases by approximately

© 2025 The Author(s). Advanced Functional Materials published by Wiley-VCH GmbH

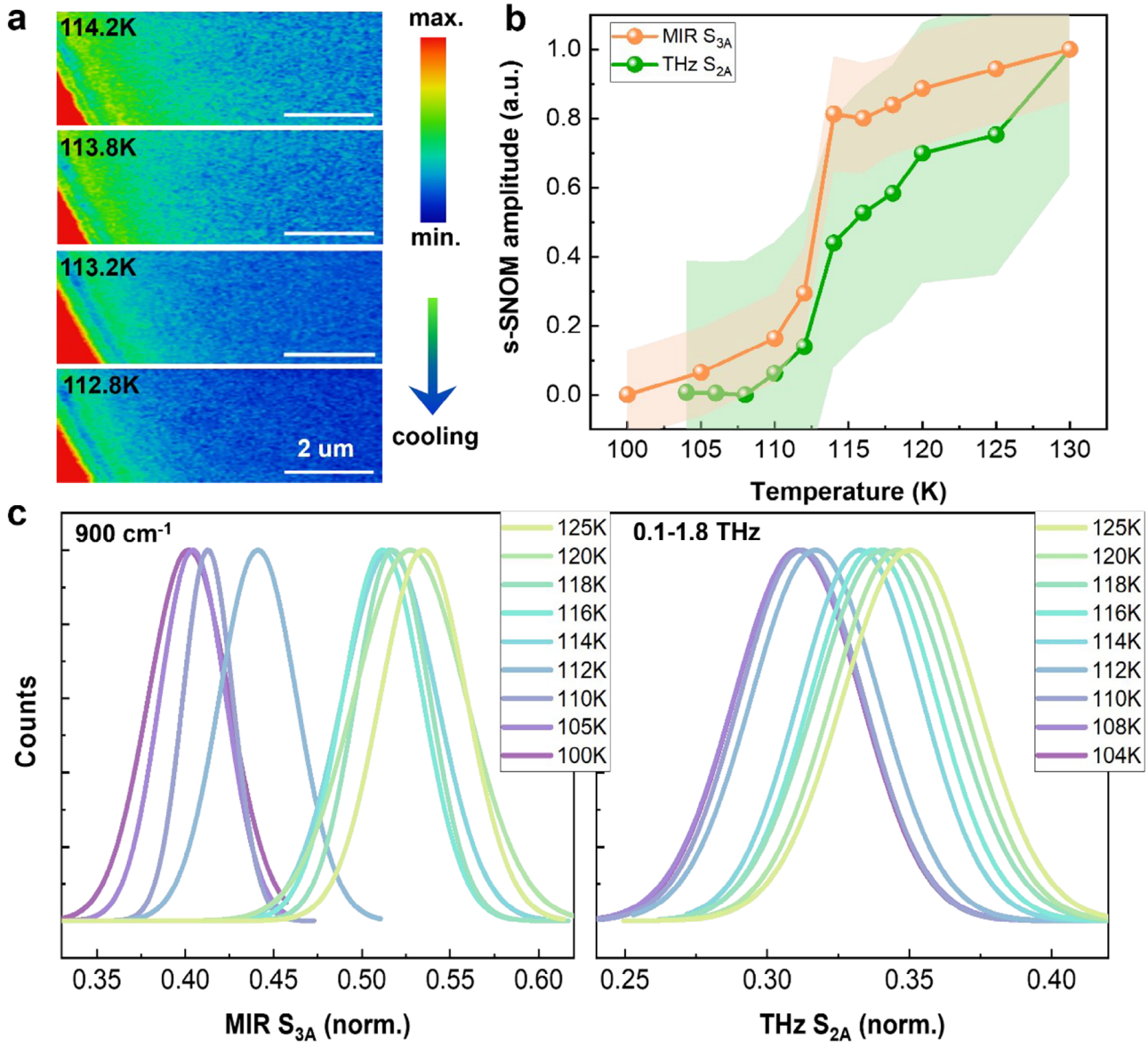

Figure 3. Low energy MIR (900 cm^{-1}) versus THz wavelength dependence of the s-SNOM amplitude across the MIT. a) 2nd order tip-demodulated THz s-SNOM amplitude images (S_{2A}). Images are normalized by a nearby graphite flake (red region in the images). The intermediary state at 113.2 K shows no island formation. b,c) MIR signal (S_{3A}) at 900 cm^{-1} and THz signal (S_{2A}) of Fe_3O_4 film versus temperature. The shaded area corresponds to the error in the averaged data (mean ± SD). b) In contrast to the MIR signal, we note that the THz signal shows a rapid increase with an increasing temperature above T_V, both experiencing a sharp drop at T_V. Below T_V, the signal remains nearly constant in both cases. MIR and THz signals are normalized to lie in the range [0, 1]. c) Gaussian distribution profiles for s-SNOM amplitude image at MIR and THz frequencies show a clear discontinuity in the intensity.

one order of magnitude below T_V (see Figure 1b). To further validate that the MIR s-SNOM amplitude change at the transition temperature during cooldown is a result of the transition, the signal is measured during the warm-up process (see SI Note 4, Supporting Information). Warming up, the MIR signal also follows a similar trend accompanied by an hysteretic behavior which is typical of a first-order transition. In contrast to the MIR signal, we note that the THz signal shows a rapid increase with increasing temperature above T_V (see Figure 3b). THz (or picosecond) pulses can effectively capture polaron-hopping, which has previously been reported to occur on picosecond timescales.[5] The observed trend indicates that at temperatures above the transition, there exists a signature of dissociated polaron domains or short-range order causing hopping-type conductivity, where thermal activation enhances polaron mobility.[21] Both MIR and THz s-SNOM signals show a comparable sharp transition in the vicinity of T_V and a tendency to demonstrate phase percolations. This can also be seen in the Gaussian distribution profiles shown in Figure 3c for MIR and THz s-SNOM images of the same area used in Figure 3b. The spread of this Gaussian reflects a combination of inherent noise, integration time and variations due to local scatterers and should not be

© 2025 The Author(s). Advanced Functional Materials published by Wiley-VCH GmbH

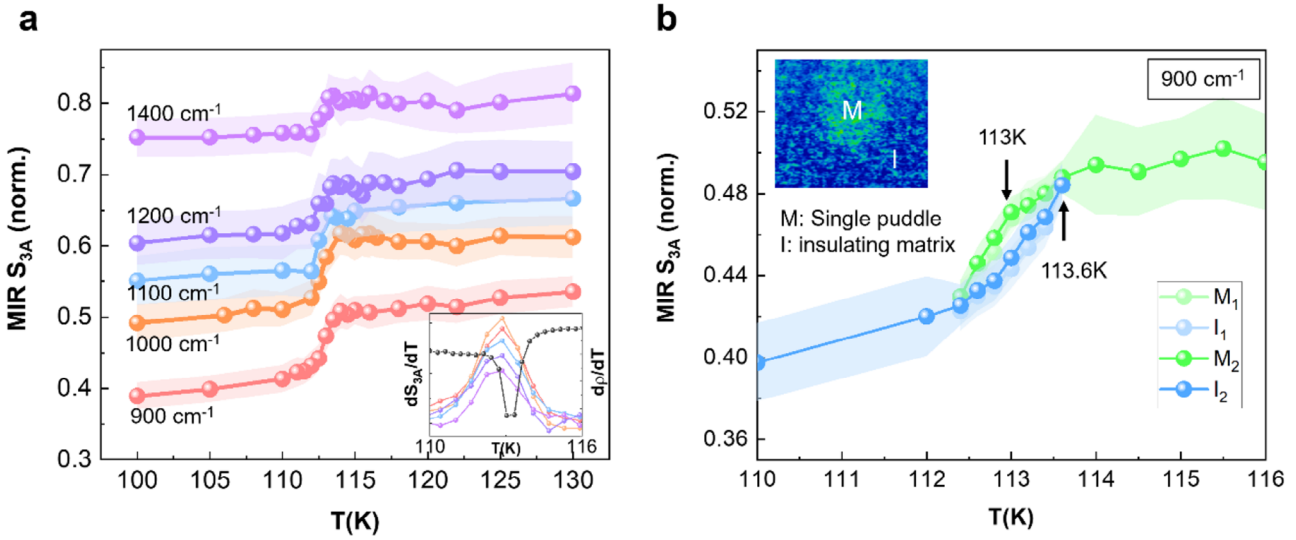

Figure 4. MIR wavelength dependence of the MIT and temperature dependence of the signal on an island versus the surrounding matrix. a) Averaged normalized s-SNOM amplitude (S_{3A}) measured at different MIR excitation frequencies while cooling down. The signal in the metallic state is higher than the insulating counterpart at all the probed frequencies. The signal displays an upward trend for a fixed temperature, accompanied by a decreasing difference between the two states at higher frequencies. The inset shows the derivative of the s-SNOM signal and resistivity with temperature. The transition width (≈2 K) as observed by s-SNOM compared to that of resistivity are well matched. b) Signal tracing for the metallic islands and the insulating matrix (see inset) during cooling through the MIT shown for two exemplary islands 1 and 2. The green (M, metallic island) and blue (I, insulating matrix) curves start from the same point (113.6 K) where the islands are yet to form; as the transition progresses, the two curves bifurcate. A slope change in the "M" curve is seen at 113 K indicating a lowering of the local transition temperature by ≈0.6 K. The shaded area corresponds to the error in the averaged data (mean ± SD).

directly interpreted as the uncertainty of the mean values plotted in Figure 3b and subsequent plots.

As discussed in the previous section on the MIR wavelength dependence based on our analytical calculations, a diminishing contrast between the metallic and insulating states is expected at higher wavenumbers up to a certain range beyond which the frequency dependence becomes non-trivial (see SI Note 5, Supporting Information). To verify the frequency dependence, we perform s-SNOM imaging at several MIR wavenumbers ranging from 900 cm^{-1} to 1400 cm^{-1}, as demonstrated in **Figure 4a**. We find that the contrast between the metallic and insulating states of Fe_3O_4 decreases with increasing excitation frequency. The contrast is particularly pronounced at lower frequencies due to an optical charge gap opening from the suppression of intra-band transitions below T_V for lower MIR frequencies that was previously observed in far-field measurements.[21,37] Above the excitation frequency of ≈1400 cm^{-1}, the metallic and insulating states have no discernable contrast. A comparison of the contrast observed at different harmonics of the s-SNOM signal across the transition indicates that at higher harmonics, there is a reduction in the signal and SNR. However, a substantial increase in the percentage change of the signal is observed (S_{2A}≈21%, S_{4A}≈30%). The higher harmonics of the s-SNOM signal originate from shallower depths, making them more surface-sensitive.[38] The enhanced contrast at higher harmonics is primarily due to effective background suppression but may also indicate surface-localized effects (see SI Note 3, Supporting Information for a comparison of different harmonics).[9,24,39,40] As illustrated in the inset to Figure 4a, the transition width, given by the derivative of the s-SNOM signal with respect to the sample temperature, is ≈2 K. This aligns closely with the width of the temperature derivative of resistivity (ρ), thus confirming that the optical signal closely tracks the MIT.

We have previously assumed that the islands are remnants of the parent metallic state. However, to understand the electronic property of the islands, tracing of the s-SNOM signal exclusively from the islands is necessary. While the average signal in Figure 4a reveals crucial information on the temperature dependence during the transition but leaves out a gray area which is the transition regime consisting of islands and the matrix, both having a different signal. To gain a clearer understanding of the temperature dependence of the MIR s-SNOM signal of the island and the matrix separately, we have acquired the signal "M", which corresponds to the central region of a metallic island, and the signal "I", which refers to the surrounding insulating matrix (see Figure 4b). The shaded area represents mean ± SD and increases beyond 112 and 114 K due to lower image integration times. This analysis has been performed for two exemplary islands and their surrounding insulating matrix. The green (M) and blue (I) curves start from the same point when the islands are yet to form, but as the transition progresses, the two curves bifurcate, both exhibiting a continuous decrease in signal but at different rates. Upon the complete disappearance of the island, the two curves merge, indicating a loss of distinct signal characteristics. Notably, the core of the island, which persists until its complete disappearance, exhibits a faster decline in signal during the transition, outpacing the rate of signal decrease observed in the film before the transition. This could possibly hint at the presence of some non-triviality in the island electronic behavior. Additionally, the M' curve has a slope variation at 113 K indicating a shift of ≈0.6 K in the local transition temperature for the island compared to the global transition temperature of the film.

© 2025 The Author(s). Advanced Functional Materials published by Wiley-VCH GmbH

3. Conclusion

In summary, high-quality Fe_3O_4 films with a prominent Verwey transition were grown by ozone MBE. s-SNOM imaging reveals a formation of a percolative network of co-existing metallic and insulating phases in the vicinity of the transition. Our results demonstrate that upon cooling, metallic islands with diffuse boundaries emerge at the same locations across repeated cooling cycles, highlighting the role of local pinning disorder in the transition. These islands exhibit radii ranging from tens of nanometers to ≈500 nm. Above the transition, the increasing THz reflectivity with increasing temperature suggests charge fluctuations happening at picosecond timescales, consistent with polaron dynamics, thereby, indicating the presence of a short-range order in the high-temperature state. This work provides new insights into the role of local defect-induced phase pinning during the Verwey transition. Beyond deepening the understanding of strongly correlated oxides, our findings emphasize the significance of nanoscale optical imaging to harness the phase change functionalities for designing reconfigurable nano-optical devices,[41,42] sensors,[43] and energy storage technologies.[44,45]

4. Experimental Section

Sample Preparation: High-quality Fe_3O_4 films were grown using a VEECO GEN 10 molecular beam epitaxy (MBE) system. The base pressure in the MBE chamber was 5×10^{-10} Torr before deposition. The MgO (100) substrates (supplied by Surface Net) are first outgassed in the load lock in a vacuum of 2×10^{-8} Torr at 200 °C to remove any contamination from the substrate surface before insertion into the growth chamber. After loading the substrate into the growth chamber, a second outgassing process was performed at a temperature of ≈800 °C in an ultra-high vacuum (UHV) environment to provide a clean and smooth surface before starting the film growth. The Fe_3O_4 film is deposited at a substrate temperature of ≈300 °C. A Knudsen cell is used for the evaporation of Fe (held at a temperature of ≈1200 °C) in the presence of ozone at a pressure of 1.1×10^{-7} Torr. The Fe_3O_4 films were deposited at a deposition rate of ≈0.05 Å s^{-1}, as measured by quartz crystal monitoring (QCM). The film thickness was then determined by X-ray reflectometry consistent with a deposition rate of Fe_3O_4 of ≈0.0526 Å s^{-1} which is in very good agreement with the QCM. After growth, the substrate is cooled down to 200 °C in the presence of ozone and then cooled down to room temperature in the absence of ozone. We conducted in situ reflection high-energy electron diffraction (RHEED) on the samples after cooling, to assess both the crystallinity and the quality of the deposited films on MgO (100) substrate. To achieve the final high quality epitaxial film of Fe_3O_4, ≈40 films were successively prepared on different substrates and under different growth conditions until the RHEED pattern indicated an optimal epitaxial growth. By varying the growth conditions the film either had a different structure (Fe_2O_3) or was comprised of more than one iron oxide phase. Finally, both RHEED and XRD indicated the successful growth of single-phase epitaxial films of Fe_3O_4 on MgO (100) substrates.

Crystal Structure: The crystal structure of the film was determined by carrying out high-resolution x-ray diffraction (HR-XRD) measurements using a four-circle goniometer and a D8 Discover-Bruker X-ray diffractometer. The diffraction patterns (see SI Note 1, Supporting Information) confirm the growth of a high-quality, single phase Fe_3O_4 film grown epitaxially on a MgO (100) single crystal substrate with no presence of any secondary phases. The thin film thickness is determined by X-ray reflectivity measurements (XRRs) to be ≈ 57 nm.

Electrical Transport: Electrical resistivity measurements were performed using a Quantum Design Dynacool physical property measurement system (PPMS). DC measurements were performed using a Keithley current source (6221) and nano-voltmeter (2182) using a Van-der Pauw method. An applied current of 100 nA was used. Electrical connections to the four corners of the unpatterned sample are made using aluminum wire-bonding. The sample becomes too insulating below ≈70 K to allow for measurements of its resistivity.

Near-Field Imaging: Near-field imaging was performed using a cryo s-SNOM from Attocube systems. Tunable MIR QCL laser (900 to 2600 cm^{-1}) was kept at a power of 0.8 mW to avoid sample damage, heating and non-linearity in the photo-detector response. A platinum-iridium coated silicon tip with a radii of ≈20 nm and a cantilever resonance frequency near 250 KHz (from NeaSpec) with a tip geometry which allowed for strong light collection,. The near-field signal decays exponentially as the tip moves away from the sample surface. Therefore, to obtain a pure near field signal from the large spurious background scattering from the tip shank, cantilever, and sample surface under direct illumination by the laser, the collected signal was demodulated to 3rd order of the tip oscillation frequency.[9] Remnant multiplicative background scattering is further eliminated through pseudo-heterodyne interferometric detection which also enables simultaneous detection of the signal amplitude and the phase information via sideband frequency lock-in detection.[24] For THz s-SNOM measurements, a broadband THz laser source (Menlo systems broadband terahertz spectrometer TeraSmart) was used which has a frequency range between 0.1 to 1.8 THz when integrated with the cryo s-SNOM and working in the near-field mode. THz tips with a tip radius of ≈40 nm made of Pt-Ir alloy were supplied from Rocky Mountain nanotechnology. The tip used for THz imaging is longer compared to the MIR tip to couple efficiently to the THz radiation by resonating with the THz peak frequency.[46] All images were normalized with a nearby graphite flake scanned along with the film region under investigation (see SI Note 7, Supporting Information on using graphite as a reference).

Image Processing: To eliminate artifacts arising in the scans from enhanced mechanical noise at low temperatures, a 2D fast Fourier transform filtering was performed on the optical scans after identifying erroneous noisy frequency spots in the 2D FFT of AFM images taken simultaneously with the s-SNOM. Image processing was carried out using the open-source software Gwyddion. For more information on the image processing, refer to SI Notes 2 and 8 (Supporting Information).

Statistical Analysis: The island size (radii) estimation shown in Figure 2f of the manuscript was carried out using a custom Python script based on a single threshold detection technique. This automated analysis was performed for several images (>10) with islands. A reverse Fourier transform was applied to some of the images for the suppression of contrast artifacts appearing near the surface terraces. Both island size with or without the terraces show a similar size distribution. The size distribution analysis excludes the outliers by discarding radii values outside the range of 10 nm to 1 µm. For visual continuity, a value of 1 was assigned to x-axis bins with zero counts. The average data points shown in Figures 3b and 4a,b were obtained by performing Gaussian fitting of the intensity histogram of the selected region within the image. The spread of the intensity or the error bar is indicated by the standard deviation ($\gamma \pm$ SD). Additional methodological details are provided in SI Notes 2 and 8 (Supporting Information).

Supporting Information

Supporting Information is available from the Wiley Online Library or from the author.

Acknowledgements

Funding by the International Max Planck Research School for Science and Technology of Nano-Systems is gratefully acknowledged. Partially funded by the Deutsche Forschungsgemeinschaft (DFG, German Research Foundation) – project no. 471731263. Funding has been provided by the Alexander von Humboldt Foundation in the framework of the Alexander von Humboldt Professorship to S.S.P.P. endowed by the Federal Ministry of Education and Research.

© 2025 The Author(s). Advanced Functional Materials published by Wiley-VCH GmbH

Conflict of Interest

The authors declare no conflict of interest.

Author Contributions

K.T. and M.I.S.M. contributed equally to this work. K.T. and S.S.P.P. designed the experiments; S.S.P.P. conceived and supervised the project; K.T., M.I.S.M., K.X., and S.S.P.P. wrote the manuscript; K.T. performed the mid-infrared and terahertz scattering scanning near field microscopy (s-SNOM) measurements with simultaneous atomic force microscopy (AFM) and electrical transport measurements, analyzed the results, and performed analytical calculations; M.I.S.M. grew and optimized the Fe_3O_4 samples, performed in situ Reflection high energy electron diffraction (RHEED), carried out the high- resolution X-ray diffraction (HR-XRD) and reflectivity measurements (XRR), performed the AFM scans and carried out the electrical transport measurements using the PPMS. MT helped in mounting the Fe source and the initial test of the Knudsen cell; K.X. helped with the data analysis and results discussion.

Data Availability Statement

The data that support the findings of this study are available from the corresponding author upon reasonable request.

Keywords

island, magnetite, metal to insulator transition, mid-infrared, polaron, scattering-type scanning near-field optical microscopy, terahertz, trimeron, verwey transition

Received: March 19, 2025
Revised: June 30, 2025
Published online:

[1] E. Morosan, D. Natelson, A. H. Nevidomskyy, Q. M. Si, *Adv. Mater.* **2012**, *24*, 4896.
[2] E. J. W. Verwey, *Nature* **1939**, *144*, 327.
[3] E. J. W. Verwey, P. W. Haayman, *Physica* **1941**, *8*, 979.
[4] M. S. Senn, J. P. Wright, J. Cumby, J. P. Attfield, *Phys. Rev. B* **2015**, *92*, 024104.
[5] S. de Jong, R. Kukreja, C. Trabant, N. Pontius, C. F. Chang, T. Kachel, M. Beye, F. Sorgenfrei, C. H. Back, B. Bräuer, W. F. Schlotter, J. J. Turner, O. Krupin, M. Doehler, D. Zhu, M. A. Hossain, A. O. Scherz, D. Fausti, F. Novelli, M. Esposito, W. S. Lee, Y. D. Chuang, D. H. Lu, R. G. Moore, M. Yi, M. Trigo, P. Kirchmann, L. Pathey, M. S. Golden, M. Buchholz, et al., *Nat. Mater.* **2013**, *12*, 882.
[6] W. Wang, J. Li, Z. X. Liang, L. J. Wu, P. M. Lozano, A. C. Komarek, X. Z. Shen, A. H. Reid, X. Wang, Q. Li, W. Yin, K. Sun, I. K. Robinson, Y. Zhu, M. P. M. Dean, J. Tao, *Sci. Adv.* **2023**, *9*, adf8220.
[7] T. Kolodziej, A. Kozlowski, P. Piekarz, W. Tabis, Z. Kakol, M. Zajac, Z. Tarnawski, J. M. Honig, A. M. Oles, K. Parlinski, *Phys. Rev. B* **2012**, *85*, 104301.
[8] X. Liu, L. Yin, W. B. Mi, *Sci. Rep.* **2017**, *7*, https://doi.org/10.1038/srep43403.
[9] R. Hillenbrand, B. Knoll, F. Keilmann, *J. Microsc.* **2001**, *202*, 77.
[10] R. Hillenbrand, Y. Abate, M. K. Liu, X. Z. Chen, D. N. Basov, *Nat. Rev. Mater.* **2025**, *10*, 285.
[11] A. Bouhelier, M. Beversluis, A. Hartschuh, L. Novotny, *Phys. Rev. Lett.* **2003**, *90*, 013903.
[12] H. T. Stinson, A. Sternbach, O. Najera, R. Jing, A. S. Mcleod, T. V. Slusar, A. Mueller, L. Anderegg, H. T. Kim, M. Rozenberg, D. N. Basov, *Nat. Commun.* **2018**, *9*, 3604.
[13] A. J. Frenzel, A. S. McLeod, D. Z.-R. Wang, Y. Liu, W. Lu, G. Ni, A. W. Tsen, Y. Sun, A. N. Pasupathy, D. N. Basov, *Phys. Rev. B* **2018**, *97*, 035111.
[14] J. Duan, A. T. Martín-Luengo, C. Lanza, S. Partel, K. Voronin, A. I. F. Tresguerres-Mata, G. Álvarez-Pérez, A. Y. Niakitin, J. Martín-Sánchez, P. Alonso-González, *Sci. Adv.* **2025**, *11*, ads0569.
[15] P. Li, I. Dolado, F. J. Alfaro-Mozaz, F. Casanova, L. E. Hueso, S. Liu, J. H. Edgar, A. Y. Nikitin, S. Vélez, R. Hillenbrand, *Science* **2018**, *359*, 892.
[16] D. W. Zhang, E. M. You, L. Wang, B. K. Jang, T. Yousaf, P. F. Zhang, J. Kim, C. H. Yang, J. Seidel, *Adv. Funct. Mater.* **2025**, *35*, 2422945.
[17] T. Janda, J. Godinho, T. Ostatnicky, E. Pfitzner, G. Ulrich, A. Hoehl, S. Reimers, Z. Šobáň, T. Metzger, H. Reichlová, V. Novák, R. P. Campion, J. Heberle, P. Wadley, K. W. Edmonds, O. J. Amin, J. S. Chauhan, S. S. Dhesi, F. Maccherozzi, R. M. Otxoa, P. E. Roy, K. Olejník, P. Němec, T. Jungwirth, B. Kaestner, J. Wunderlich, *Phys. Rev. Mater.* **2020**, *4* , 094413.
[18] A. J. Huber, F. Keilmann, J. Wittborn, J. Aizpurua, R. Hillenbrand, *Nano Lett.* **2008**, *8*, 3766.
[19] T. L. Cocker, V. Jelic, R. Hillenbrand, F. A. Hegmann, *Nat. Photonics* **2021**, *15*, 558.
[20] W. J. Deng, Y. N. Wang, X. Y. Zhu, R. Xin, T. X. Li, Q. C. Weng, W. Lu, *ACS Photonics* **2025**, *12*, 2187.
[21] L. V. Gasparov, D. B. Tanner, D. B. Romero, H. Berger, G. Margaritondo, L. Forró, *Phys. Rev. B* **2000**, *62*, 7939.
[22] M. S. Senn, J. P. Wright, J. P. Attfield, *Nature* **2012**, *481*, 173.
[23] X. H. Liu, C. F. Chang, A. D. Rata, A. C. Komarek, L. H. Tjeng, *npj Quantum Mater.* **2016**, *1*, 16027.
[24] N. Ocelic, A. Huber, R. Hillenbrand, *Appl. Phys. Lett.* **2006**, *89*, 101124.
[25] R. Prozorov, M. A. Tanatar, E. I. Timmons, M. Konczykowski, T. Prozorov, *Mater. Res. Bull.* **2023**, *167*, 112442.
[26] N. Fominykh, V. Stegailov, *Phys. Rev. B* **2025**, *111*, 115130.
[27] Z. Wang, A. C. Bovik, H. R. Sheikh, E. P. Simoncelli, *IEEE Trans. Image Process.* **2004**, *13*, 600.
[28] W. Luo, M. Boselli, J.-M. Poumirol, I. Ardizzone, J. Teyssier, D. van der Marel, S. Gariglio, J.-M. Triscone, A. B. Kuzmenko, *Nat. Commun.* **2019**, *10*, 2774.
[29] B. Hauer, A. P. Engelhardt, T. Taubner, *Opt. Express* **2012**, *20*, 13173.
[30] T.-H. Kim, M. Angst, B. Hu, R. Jin, X.-G. Zhang, J. F. Wendelken, E. W. Plummer, A.-P. Li, *Proc. Natl. Acad. Sci. U S A* **2010**, *107*, 5272.
[31] K. J. Lai, M. Nakamura, W. Kundhikanjana, M. Kawasaki, Y. Tokura, M. A. Kelly, Z. X. Shen, *Science* **2010**, *329*, 190.
[32] A. Pimenov, S. Tachos, T. Rudolf, A. Loidl, D. Schrupp, M. Sing, R. Claessen, V. A. M. Brabers, *Phys. Rev. B* **2005**, *72*, 035131.
[33] R. A. Kaindl, R. D. Averitt, in *Terahertz Spectroscopy- Principles and Applications*, 1st Edition (Ed: S. L. Dexheimer) CRC Press, Boca Raton, FL, **2008**, p. 119.
[34] S. D. Conradson, S. M. Gilbertson, S. L. Daifuku, J. A. Kehl, T. Durakiewicz, D. A. Andersson, A. R. Bishop, D. D. Byler, P. Maldonado, P. M. Oppeneer, J. A. Valdez, M. L. Neidig, G. Rodriguez, *Sci. Rep.* **2015**, *5*, 15278.
[35] J. A. Spies, J. Neu, U. T. Tayvah, M. D. Capobianco, B. Pattengale, S. Ostresh, C. A. Schmuttenmaer, *J. Phys. Chem. C* **2020**, *124*, 22335.
[36] R. Ulbricht, E. Hendry, J. Shan, T. F. Heinz, M. Bonn, *Rev. Mod. Phys.* **2011**, *83*, 543.
[37] A. Schlegel, S. F. Alvarado, P. Wachter, *J Phys. C: Solid State* **1979**, *12*, 1157.

© 2025 The Author(s). Advanced Functional Materials published by Wiley-VCH GmbH

[38] A. A. Govyadinov, S. Mastel, F. Golmar, A. Chuvilin, R. S. Carney, R. Hillenbrand, *ACS Nano* **2014**, *8*, 6911.
[39] B. Knoll, F. Keilmann, *Opt. Commun.* **2000**, *182*, 321.
[40] J. M. Atkin, S. Berweger, A. C. Jones, M. B. Raschke, *Adv. Phys.* **2012**, *61*, 745.
[41] M. Wuttig, H. Bhaskaran, T. Taubner, *Nat. Photonics* **2017**, *11*, 465.
[42] S. Jana, K. V. Sreekanth, O. A. M. Abdelraouf, R. H. Lin, H. Liu, J. H. Teng, R. Singh, *Nano Lett.* **2024**, *24*, 3922 .
[43] M. Cotrufo, S. B. Sulejman, L. Wesemann, M. A. Rahman, M. Bhaskaran, A. Roberts, A. Alù, *Nat. Commun.* **2024**, *15*, 4483.
[44] Y. Xing, Y. Q. Fan, J. J. Wang, M. Wang, Q. Y. Xuan, Z. P. Ma, W. F. Guo, L. Mai, *ACS Nano* **2024**, *18*, 18444.
[45] K. Matuszek, M. Kar, J. M. Pringle, D. R. MacFarlane, *Chem. Rev.* **2023**, *123*, 491.
[46] F. Huth, A. Chuvilin, M. Schnell, I. Amenabar, R. Krutokhvostov, S. Lopatin, R. Hillenbrand, *Nano Lett.* **2013**, *13*, 1065.

© 2025 The Author(s). Advanced Functional Materials published by Wiley-VCH GmbH